International Journal of Biological Macromolecules 277 (2024) 134411

Contents lists available at ScienceDirect

International Journal of Biological Macromolecules

journal homepage: www.elsevier.com/locate/ijbiomac

PRMT1 and TDRD3 promote stress granule assembly by rebuilding the protein-RNA interaction network

Mengtong Qin [a,b,1], Weiwei Fan [a,1], Linge Li [a,d,1], Tian Xu [a,1], Hanyu Zhang [a], Feng Chen [a], Jingwen Man [a,b], Arnaud John Kombe Kombe [e], Jiahai Zhang [a], Yunyu Shi [a], Xuebiao Yao [a], Zhenye Yang [a,*], Zhonghuai Hou [a,d,*], Ke Ruan [a,c,*], Dan Liu [a,b,c,*,2]

[a] MOE Key Laboratory for Membraneless Organelles and Cellular Dynamics, Hefei National Research Center for Physical Sciences at the Microscale, Division of Life Sciences and Medicine, University of Science and Technology of China, Hefei, 230027, China
[b] The CAS Key Laboratory of Innate Immunity and Chronic Disease, School of Basic Medical Sciences, Division of Life Sciences and Medicine, University of Science and Technology of China, Hefei 230027, China
[c] The First Affiliated Hospital of University of Science and Technology of China, Division of Life Sciences and Medicine, University of Science and Technology of China, Hefei 230001, China
[d] Department of Chemical Physics, iChEM, University of Science and Technology of China, Hefei 230026, China
[e] Division of Infectious Diseases and Geographic Medicine, Department of Internal Medicine, University of Texas Southwestern Medical Center, Dallas, TX 75390, USA

ARTICLE INFO

Keywords:
TDRD3
PRMT1
Stress granule
Liquid-liquid phase separation
Asymmetric dimethylarginine

ABSTRACT

Stress granules (SGs) are membrane-less organelles (MLOs) or cytosolic compartments formed upon exposure to environmental cell stress-inducing stimuli. SGs are based on ribonucleoprotein complexes from a set of cytoplasmic proteins and mRNAs, blocked in translation due to stress cell-induced polysome disassembly. Post-translational modifications (PTMs) such as methylation, are involved in SG assembly, with the methylation writer PRMT1 and its reader TDRD3 colocalizing to SGs. However, the role of this writer-reader system in SG assembly remains unclear. Here, we found that PRMT1 methylates SG constituent RNA-binding proteins (RBPs) on their RGG motifs. Besides, we report that TDRD3, as a reader of asymmetric dimethylarginines, enhances RNA binding to recruit additional RNAs and RBPs, lowering the percolation threshold and promoting SG assembly. Our study enriches our understanding of the molecular mechanism of SG formation by elucidating the functions of PRMT1 and TDRD3. We anticipate that our study will provide a new perspective for comprehensively understanding the functions of PTMs in liquid-liquid phase separation driven condensate assembly.

1. Introduction

Multivalent interactions between cell biomacromolecules, including proteins and RNAs, are responsible for membrane-less organelles (MLOs) formation through liquid-liquid phase separation (LLPS), which, in turn, creates independent cytosolic compartments for biochemical reactions [1–7]. Specifically, protein-protein interactions involve multiple folded domains [8,9] or intrinsic-disordered regions (IDRs) of two or multiple prion-like proteins [10,11] that are responsible for driving LLPS or gelation of these proteins. Besides, RNA-protein interactions include RNA-binding proteins (RBPs) and RNAs [9,12,13] that form interacting networks based on the binding of RNA-recognition motif (RRM) [14] or positively charged Arg-Gly-Gly (RGG) motifs and RNAs [15]. Moreover, interactions between RNAs, also known as RNA self-assembly, facilitate biomacromolecule aggregations and participate in cytoplasm and nucleoplasm cell organization [16,17].

Among the MLOs formed through biomacromolecule interactions, stress granules (SGs) count for an important proportion and are notably induced in response to external stresses, including heat shock, oxidative stress, or osmotic stress [18–22]. More importantly, by constantly exchanging components with the cytoplasm, formed SGs help restore cell redox homeostasis and participate in the healing process after stress

* Corresponding authors at: MOE Key Laboratory for Membraneless Organelles and Cellular Dynamics, Hefei National Research Center for Physical Sciences at the Microscale, Division of Life Sciences and Medicine, University of Science and Technology of China, Hefei, 230027, China.
E-mail addresses: zhenye@ustc.edu.cn (Z. Yang), hzhlj@ustc.edu.cn (Z. Hou), kruan@ustc.edu.cn (K. Ruan), dliu919@ustc.edu.cn (D. Liu).
[1] These authors contributed equally to this work.
[2] Lead Contact.

https://doi.org/10.1016/j.ijbiomac.2024.134411
Received 9 April 2024; Received in revised form 27 May 2024; Accepted 31 July 2024
Available online 2 August 2024

removal [23,24]. In normal circumstances and when the antioxidant response is well-regulated, the formation of SGs is transient and for a short duration. After the restoration of the cell stress homeostasis, SGs disassemble [25]. Thus, mutation-associated dysregulations affecting the formation and disassembly of SGs are detrimental to the cells and have been associated with neurodegenerative diseases [26,27], cancer [28–32], and the aberrant/uncontrolled replication of viruses [33].

Understanding the assembly and composition of SGs has initiated concurrent studies since SG assembly-disassembly pathway might constitute a therapeutic target against several pathological conditions. SGs are dynamic MLOs containing a large amount of untranslated mRNAs. Their main structure consists of an inner core with higher proteins and mRNA concentrations and a surrounding shell with lower protein and mRNA concentrations, responsible for the SGs' dynamism [34]. The mRNA components of SGs originate from the cytosolic compartment and are mainly involved in the multivalent interactions with RBPs. They represent the leading cause of SG formation [35–37]. Indeed, proteomics studies have identified several molecular factors involved in the formation of SGs, including G3BP1, which binds to the released mRNAs in the cytoplasm and triggers the assembly of SGs [38]. The ubiquitination, removal, or knockdown of G3BP1 weakens the driving force within the network under the percolation threshold that reduces the formation of SGs, indicating that G3BP1 plays a crucial regulatory role in post-translational modifications (PTMs) necessary for SG assembly [39].

Protein arginine methyltransferase 1 (PRMT1), a type I methyltransferase catalyzing the formation of asymmetric dimethylarginine (ADMA), is found to be localized in arsenite-induced SGs and methylated G3BP1 [40], TOP3B [41] and possibly other SG constituent proteins. The ADMAs will be recognized by Tudor domain containing

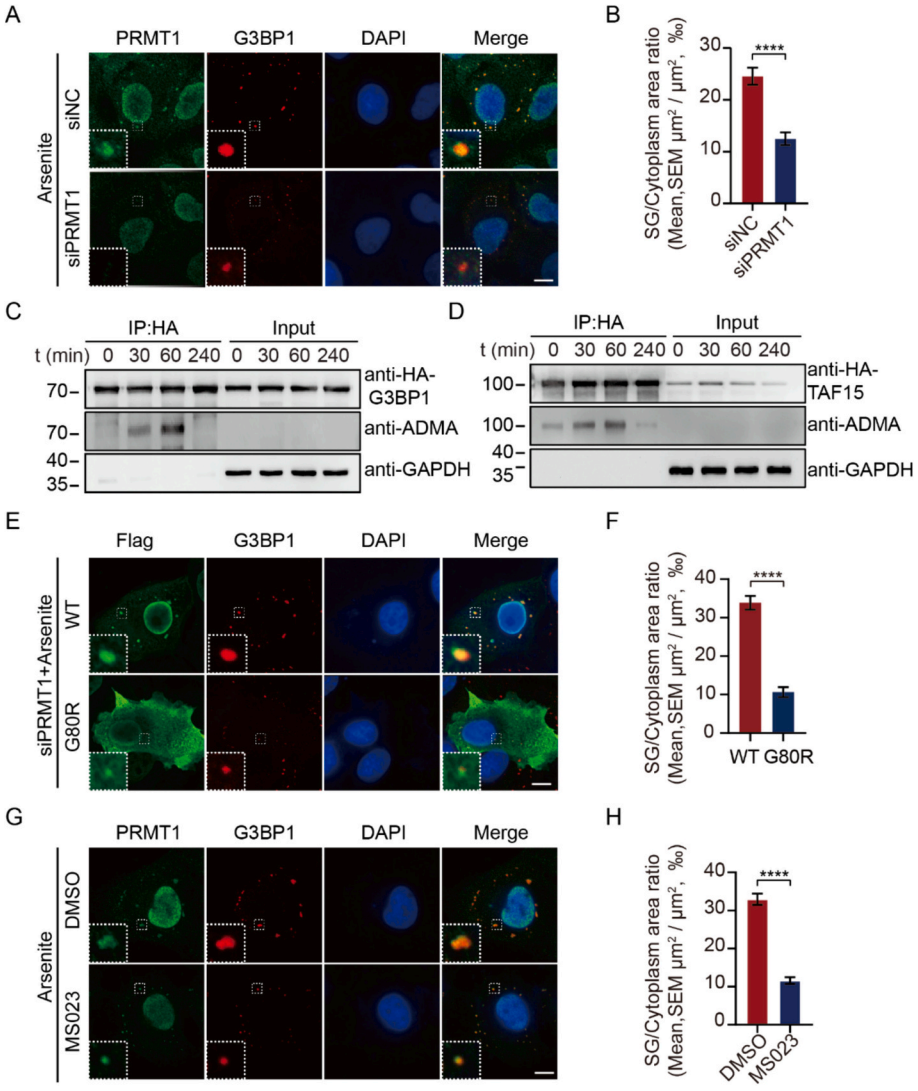

Fig. 1. PRMT1 plays a crucial role in SG assembly.
(A, B) SG formation in U2OS cells with PRMT1 knockdown by siRNA. Immunofluorescence and quantitative analysis of SG assembly by staining endogenous G3BP1 and PRMT1 with corresponding antibodies in U2OS cells. Cells were stressed by sodium arsenite (500 μM; 60 min). Representative images are shown in A. The SG area ratio (SG area to cytoplasm area) was quantified in B. Scale bar, 20 μm. Error bars indicate SEM. $N \geq 20$ cells per condition. (C, D) Western blot analysis of ADMA modifications of immunoprecipitation HA-G3BP1 (C) or HA-TAF15 (D). Samples were obtained according to the time points shown in S1B. (E, F) SG formation in PRMT1 knockdown U2OS cells with PRMT1 enzyme activity deficient mutation. Cells expressing Flag-PRMT1 or Flag-PRMT1 G80R were treated with sodium arsenite (500 μM; 60 min), and stained for Flag and G3BP1. Representative images are shown in E. The SG area ratio was quantified in F. Scale bar, 20 μm. Error bars indicate SEM. $N \geq 20$ cells per condition. (G, H) SG formation in U2OS cells with inhibitor MS023.SG assembly and colocalization analysis by immunofluorescence staining of G3BP1 plus PRMT1 in U2OS cells. DMSO and type I protein arginine methyltransferases inhibitor, MS023 (50 μM; 48 h) treated U2OS cells were compared and cells were stressed by sodium arsenite (500 μM; 60 min) prior to immuno-staining. Representative images are shown in G. The SG area ratio was quantified in H. Scale bar, 10 μm. Error bars indicate SEM. $N \geq 20$ cells per condition.

proteins subsequently [42]. One of these ADMA readers, TDRD3 [41,43,44], localizes to SGs *via* its Tudor domain [45] and recruits methylated TOP3B [41]. PRMT1 and TDRD3 form a methylation "writing" and "reading" system. However, the potential function of this system in SGs remains elusive.

Here, we demonstrated that PRMT1 catalyzes the formation of ADMA for methylation of SG G3BP1. Also, we showed that TDRD3 binds directly to G3BP1 and bridges the methylated G3BP1 and RNAs. Coarse-grained simulation and LLPS assays *in vitro* demonstrate that two or more TDRD3 molecules recruited by multiple ADMA sites on G3BP1 increase the valence of the percolation network and promote LLPS. Our findings establish a coherent framework for SG assembly, providing a reference for other studies on PTM-regulated assembly mechanisms of MLOs.

2. Results

2.1. PRMT1 promotes the assembly of SGs in U2OS cells

It has previously been reported that PRMT1 colocalizes with arsenite-induced SGs marked by G3BP1 [38]. To assess whether PRMT1 is involved in SG assembly, we knocked down PRMT1 using siRNA. As expected, we found a reduction in the ratio of G3BP1-marked SG area to cytoplasmic area (SG area ratio) in stressed U2OS cells (Figs. 1A and B, S1A). The area ratio is widely used to quantify the formation of droplets in cells [46–50]. Therefore, the decrease in the SG area ratio demonstrated the inhibition of SG assembly. PRMT1 is known to catalyze the formation of ADMA in RGG motifs, and many RBPs contain RGG motifs in SGs [15]. To verify whether ADMA occurs universally in SG constituent proteins, we studied five proteins containing RGG motifs, including G3BP1, TAF15, DDX3X, Caprin1, and UBAP2. We overexpressed these five proteins and enriched them at different time points after arsenite stress, as shown in Fig. S1B by immunoprecipitation (Figs. 1C and D, S1C-E). Additionally, the assembly and disassembly of SGs at different time points within the cells were assessed (Fig. S1F—I). We found that all proteins were methylated during arsenite stress, and the ADMA level decreased with SG disassembly when arsenite was washed out(Figs. 1C and D, S1C-E). This result suggested that PRMT1 may play a crucial role in catalyzing formation of ADMA during SG assembly. Therefore, the wild type (WT) and enzyme activity deficient mutant (G80R) of PRMT1 [51,52] were rescued into PRMT1-knocked-down cells, respectively (Figs. 1E and F, S1J and K). Both were recruited into arsenite-induced SG assembly, but the G80R mutant did not restore the SG area ratio as the WT-PRMT1 did (Fig. 1E and F). Meanwhile, we treated cells with type I protein arginine methyltransferase inhibitor, MS023, and found similar phenotypes as PRMT1 knockdown (Fig. 1G and H). These results indicate that PRMT1 plays the role of a "writer" within SGs, orchestrating the methylation events that are crucial for SG assembly.

2.2. TDRD3 recognizes and binds with methylated G3BP1 to promote SG assembly

TDRD3 is known as an ADMA reader [43,53] and localizes around SGs [41,45,54]. We knocked down TDRD3 in U2OS cells to evaluate its

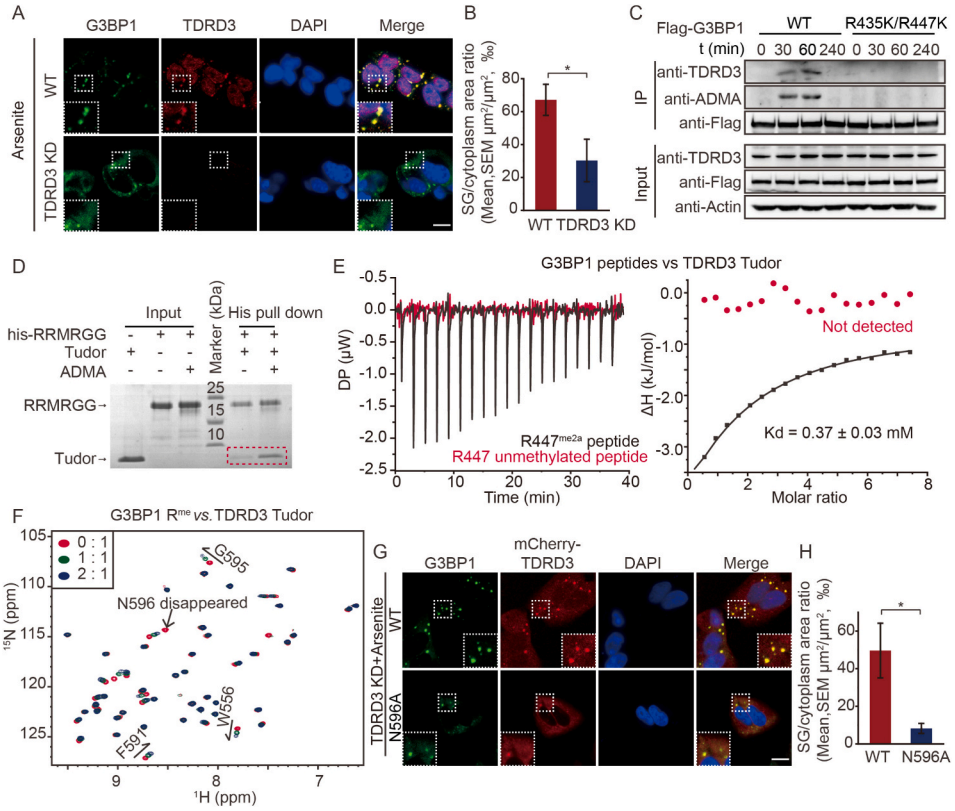

Fig. 2. TDRD3-methylated G3BP1 interaction is essential for SG assembly.
(A, B) SG formation in U2OS cells with TDRD3 knockdown by shRNA. Representative images are shown in A. The SG area ratio was quantified in B. Scale bar, 20 μm. Error bars indicate SEM. N ≥ 20 cells per condition. (C) Western blot analysis of ADMA modification of Flag-G3BP1 transfected into U2OS cells was detected using corresponding antibodies. TDRD3 was immunoprecipitated with G3BP1. Samples were obtained according to the time points shown in S1B. (D) His-pull-down of the methylated or unmethylated G3BP1 RRM-RGG with TDRD3 Tudor domain. The gel was stained by Coomassie blue. (E) ITC results of unmethylated and methyalted G3BP1 peptides titrating to 0.1 mM TDRD3 Tudor. (F) N596 residue of TDRD3 Tudor domain is essential for recognizing G3BP1 R^{me}. (G, H) SG formation in TDRD3 knockdown U2OS cells with TDRD3 ADMA binding site mutation. Cells expressing mCherry-TDRD3 were treated with sodium arsenite (500 μM; 60 min), and stained for G3BP1. Representative images are shown in G. The SG area ratio was quantified in H. Scale bar, 20 μm. Error bars indicate SEM. N ≥ 20 cells per condition.

contribution to SG assembly (Fig. S2A). As expected, we found a decreased SG area ratio in TDRD3-knocked-down stressed cells (Fig. 2A and B). Then, we assessed and detected the interaction between methylated G3BP1 and TDRD3 in cells by immunoprecipitation. TDRD3 interacted with methylated G3BP1, not the mutant G3BP1 (R435K/R447K), which cannot be methylated by PRMT1 (Fig. 2C). We also tested the binding ability of the TDRD3 Tudor domain to the G3BP1 RRM-RGG region by pull-down assay. The TDRD3 Tudor domain showed higher affinity to the methylated G3BP1 RRM-RGG than the unmethylated one (Figs. 2D, S2A). This result was further confirmed by isothermal titration calorimetry (ITC) assays, which demonstrated that the unmethylated G3BP1 peptide did not bind to the TDRD3 Tudor domain. In contrast, the R447^{me2a} peptide exhibited an affinity with a dissociation constant (K_d) of 0.37 ± 0.03 mM (Fig. 2E), which was consistent with our previous nuclear magnetic resonance (NMR) titration result (K_d = 0.35 ± 0.01 mM) [55]. To find the key residue of the TDRD3 Tudor domain for binding methylated G3BP1 RRM-RGG, we used NMR to reveal details of the interaction. We titrated methylated G3BP1 RRM-RGG (G3BP1 R^{me}) to the TDRD3 Tudor domain and analyzed the chemical shift perturbations (CSPs) of the TDRD3 Tudor domain. The assignment results of the TDRD3 Tudor domain were from a previous study [56] (BMRB Entry:18490), and N596 of the TDRD3 Tudor domain disappeared during the titration (Fig. 2F), indicating its relevance for binding G3BP1 R^{me}. We also assessed and demonstrated that the N596A mutant of the TDRD3 Tudor domain did not bind to methylated G3BP1 peptide as in our previous study [55]. The rescued wild-type TDRD3 and N596A mutant were recruited into arsenite-induced SGs in TDRD3-knocked-down cells, but the N596A mutant did not restore the SG area ratio as the WT-TDRD3 did (Fig. 2G and H). These results indicated that the interaction between TDRD3 and methylated G3BP1 was necessary for SG assembly.

2.3. TDRD3 reconstitutes the methylated G3BP1-RNA interaction to enhance their LLPS

The formation of SGs relies on the multivalent interaction between G3BP1 and RNAs, which also drives LLPS when G3BP1 and RNAs are mixed *in vitro* [38]. The RGG motif of G3BP1 interacts with RNAs through its positive charges [15], and this RGG-RNA interaction may be blocked by methylating arginine and covering these sites with the TDRD3 Tudor domain. TDRD3 seems to act as a "cap" to reduce the valence in the interaction network modeled in a previous study [57]. However, our *in vitro* phase separation assay showed that although the ADMA modification of G3BP1 RRM-RGG significantly reduced the LLPS ability of G3BP1 and RNAs (Fig. 3A and B), the introduction of the TDRD3 Tudor domain completely restored and even further enhanced the phase separation ability of methylated G3BP1 and RNAs, with little effect on the phase separation ability of non-methylated G3BP1 RRM-RGG and RNAs (Fig. 3A and B). Increasing the concentration of the TDRD3 Tudor domain or the ratio of G3BP1 R^{me} promoted the system to undergo stronger phase separation in a dose-dependent manner (Fig. S3A—D). Furthermore, TDRD3 did not form LLPS with methylated G3BP1 without RNAs (Fig. 3C). These results suggested that TDRD3 may function as a bound-bridge, linking methylated G3BP1 and RNAs together. To verify this speculation, we titrated three different RNAs, Poly A, Poly C, and Poly U, to the TDRD3 Tudor domain (Fig. S3E-G). The CSPs of the TDRD3 Tudor domain perturbed by RNAs suggested that RNA interfered with some residues on the back of the aromatic cage of the TDRD3 Tudor domain, such as E578 and K590 (Figs. 3D, S3H), indicating that the Tudor domain of TDRD3 built a bridge between methylated G3BP1 and RNAs. Mutations in the RNA-binding sites, E578A/K590A, or the key ADMA-binding site N596A in the TDRD3 Tudor domain attenuated the LLPS of G3BP1-TDRD3-RNA (Fig. 3E).

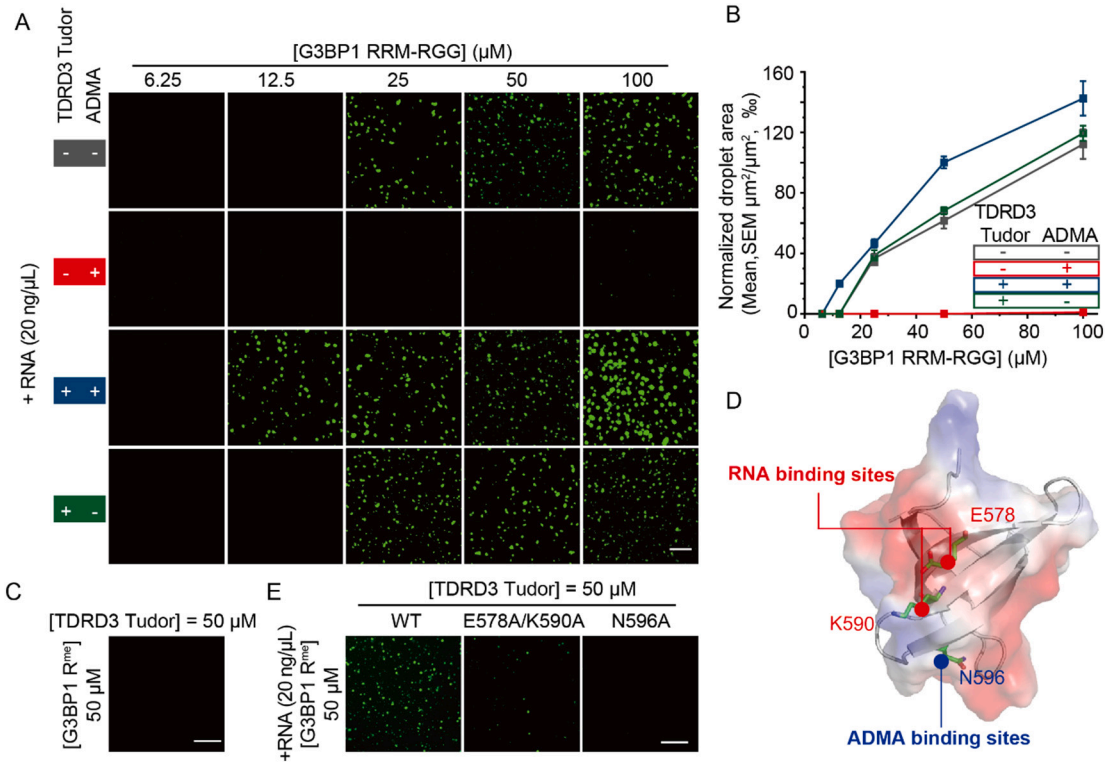

Fig. 3. TDRD3 facilitates LLPS by remodeling methylated G3BP1-RNA interactions.
(A, B) LLPS of the methylated or unmethylated G3BP1 RRM-RGG (±ADMA) with or without the TDRD3 Tudor domain (50 μM). Total RNA, 20 ng/μL. Scale bar, 20 μm. The droplets ratio was quantified and presented in B, n = 16. Error bars indicate SEM. (C) A mixture of methylated G3BP1 RRM-RGG (R^{me}, 50 μM) and TDRD3 Tudor domain (50 μM). (D) Mapping the key residues for Tudor-ADMA and Tudor-RNA interactions respectively on the crystal image of TDRD3 Tudor (PDB ID: 5YJ8). (E) LLPS of methylated G3BP1-RNA (50 μM) with the wild-type or two functionally deficient mutants of the TDRD3 Tudor domain (50 μM). RNA, 20 ng/μL. Scale bar, 20 μm.

These results suggested that TDRD3 reconstitutes the interactions between methylated RGGs on G3BP1 and RNAs, enhancing the ability of G3BP1 to form LLPS with RNAs.

2.4. TDRD3 increased the interaction valence within the percolation system

The G3BP1-TDRD3-RNA system, a percolation system [5,58–60], showed a lower percolation threshold of G3BP1 concentration (Fig. 3A). We also found that the two-site (R435 and R447) methylated G3BP1 peptide was able to bind two TDRD3 Tudor domains simultaneously in our previous work [55]. Thus, we inferred that it would modify the existing valence of the interaction network when multiple TDRD3 molecules bound to the methylated G3BP1 and bridged the ADMA-RNA interactions, theoretically changing the percolation threshold. To test our speculations, we established a coarse-grained simulation model. Rigid patchy colloids were used to model folded TDRD3 Tudor domains and G3BP1 RRM domains with surfaces annotated by interaction sites identified from NMR CSPs (Fig. S4A-C) and verified by corresponding mutations (Fig. S4D), similar to what we did on the TDRD3 Tudor domain (Figs. S2C, 3E, S3H). By the way, we referred to the assignment of the G3BP1 RRM domain from our previous study [61] (BMRB Entry: 51133). The flexible RNA and G3BP1 RGG region models were based on nucleotide or amino acid residues. In the simulations, each arginine on the RGG region formed an interaction site with RNA, whereas TDRD3 bound to methylated R435 and R447, providing more RNA-binding sites and representing an increase in the number of interaction sites with RNA after ADMA recognition by TDRD3s (Fig. 4A).

We simulated four different conditions at different G3BP1 concentrations corresponding to unmethylated G3BP1-RNA system, methylated G3BP1-RNA system, unmethylated G3BP1-TDRD3-RNA system, and methylated G3BP1-TDRD3-RNA system (Fig. 4A). To determine the LLPS capacity, we analyzed the size of clusters formed by protein and RNA at equilibrium (Fig. 4B). Our simulations showed that the size of clusters increased with increasing concentrations of G3BP1. The introduction of RGG methylation reduced the size of clusters, and the further introduction of TDRD3 significantly increased the size of clusters. However, the introduction of TDRD3 in the unmethylated system did not cause significant changes in the clusters (Fig. 4C). The trend of the cluster size agreed with the experimental data on phase separation (Fig. 3A). The simulation results suggested that the increase in RNA-binding sites at the RGG domain of G3BP1 can effectively enhance the phase separation ability of the G3BP1-RNA system.

To further confirm this idea, we fused two TDRD3 Tudor domains to form a tandem Tudor chimera (TTC). The TTC would increase RNA-binding sites when Tudor recognizes ADMA on G3BP1 by different means (Fig. 4D). Our experimental results from *in vitro* assay showed that in the methylated G3BP1-RNA system, the TTC exhibited a stronger LLPS ability compared to a single Tudor domain with the same number of TDRD3 Tudor domains (Fig. 4E and F).

In conclusion, TDRD3 reconstructed a stronger interaction network of G3BP1 and RNA by increasing RNA-binding sites, promoting the ability of this system to undergo stronger phase separation under methylated conditions.

3. Discussion

Cytoplasmic stress granules (SGs) play a critical role in antioxidative stress responses and are formed through a liquid-liquid phase separation (LLPS) by RNA-binding proteins (RBPs) that harbor low-complexity sequence domains [62]. Cytosolic molecular factors, including G3BP1 and PRMT1, respectively interacting with mRNAs catalyzing the formation of asymmetric dimethylarginine (ADMA), are involved in the assembly of SGs [38,39]. Despite its involvement in SG activation, the potential function of PRMT1 and its "reader" TDRD3 in SG assembly requires more investigation.

In this study, we found that PRMT1 and TDRD3, functioning as ADMA writer and reader respectively, promoted SG assembly in cells stimulated by arsenite. Our *in vitro* LLPS assay revealed that methylation of G3BP1 weakened its phase separation ability with RNA (Fig. 3A, line 2). This result is consistent with a previous study, reporting that demethylation of G3BP1 promotes SG assembly [40]. However, the additional TDRD3 Tudor domain boosted the LLPS of methylated G3BP1 and RNAs (Fig. 3A, line 3). TDRD3 is crucial for SG assembly (Fig. 2A) and recruits other RNA-binding proteins such as TOP3B [41]. These results suggest that SG assembly involves complex conditions [34,35,63]. The amount of SGs decreased 30 min after arsenite stress while the size and area ratio kept increasing during SG assembly (Fig. S1F—I), which may lead to bias when using quantity alone to measure the formation of SGs.

Additionally, studies are showing the diversity of SGs. Heat shock and stimulation with sorbitol of G3BPs-knock-down cells still form SG-like foci marked by FXR1 or EIF4G while arsenite, clotrimazole, and rocaglamide A did not [64]. Overexpressed TDRD3 formed SG-like foci containing type-I interferon effectors in cells without G3BPs [65]. SGs can even be "hijacked" by viruses to participate in their transcription and translation [33,66]. These findings indicate that various functional SGs may contain unique component networks, the dysregulation of which would lead to diseases [67]. The methylation system, including PRMT1 and TDRD3, may constitute one of the mechanisms by which SGs recruit different components to serve functions during cell stress. Furthermore, the diversity of SGs observed across various cell types presents a significant challenge to the study of SG regulation and the development of therapeutic strategies for related diseases.

SGs are associated with a variety of neurodegenerative diseases such as Alzheimer's disease (AD), lateral sclerosis of the spinal cord (ALS), and Parkinson's disease (PD) [5,68–72]. However, the intrinsic-disordered regions (IDRs)-driven, weak, and multivalent interactions, which form droplets or amyloid precipitates, are difficult to target and regulate by small molecules due to the lack of structural binding pockets. The molecular mechanism revealed in this study that PRMT1 and TDRD3 promoted SG assembly by rebuilding protein-RNA interaction, which provided a mechanistic basis and potential targets for developing drugs for diseases caused by abnormal SGs.

4. Conclusion

In summary, we report that ADMA formation frequently occurs on RGG-containing RBPs in SGs, which is essential for integrated SG assembly. Subsequently, PRMT1 methylates adjacent RGGs on G3BP1, providing multiple Tudor-binding sites to recruit TDRD3. TDRD3 enhanced the protein-RNA interaction by recognizing multiple ADMAs on RBPs like G3BP1, lowering the percolation threshold of LLPS, and finally promoting the assembly of SGs. (Fig. 4G).

5. Materials and methods

5.1. Cell culture and transfection

U2OS cells and HEK293T cells were cultured in DMEM supplemented with 10 % fetal bovine serum and 1 % penicillin-streptomycin at 37 °C with 5 % CO_2. Cells were transfected with plasmid DNA using Lipofectamine 3000 (Thermo Fisher Scientific, Shanghai, China). The shRNA oligonucleotide sequence for TDRD3 was 5'-CCGGGCAGTGGATTACCTAGAAATACTCGAGTATTTCTAGGTAATCCA.

CTGCTTTTTG-3′ oligonucleotides. The siRNA oligonucleotide sequence for PRMT1 was 5'-GCCAACAAGUUAGACCACGTT-3′ (synthesized by GenePharma) [73,74].

For overexpression of WT and mutated proteins after siRNA treatment, cells were initially transfected with siRNA. Eight hours later, they were further transfected with either Flag-PRMT1 or the Flag-PRMT1 G80R. The cells were then collected for subsequent experimental

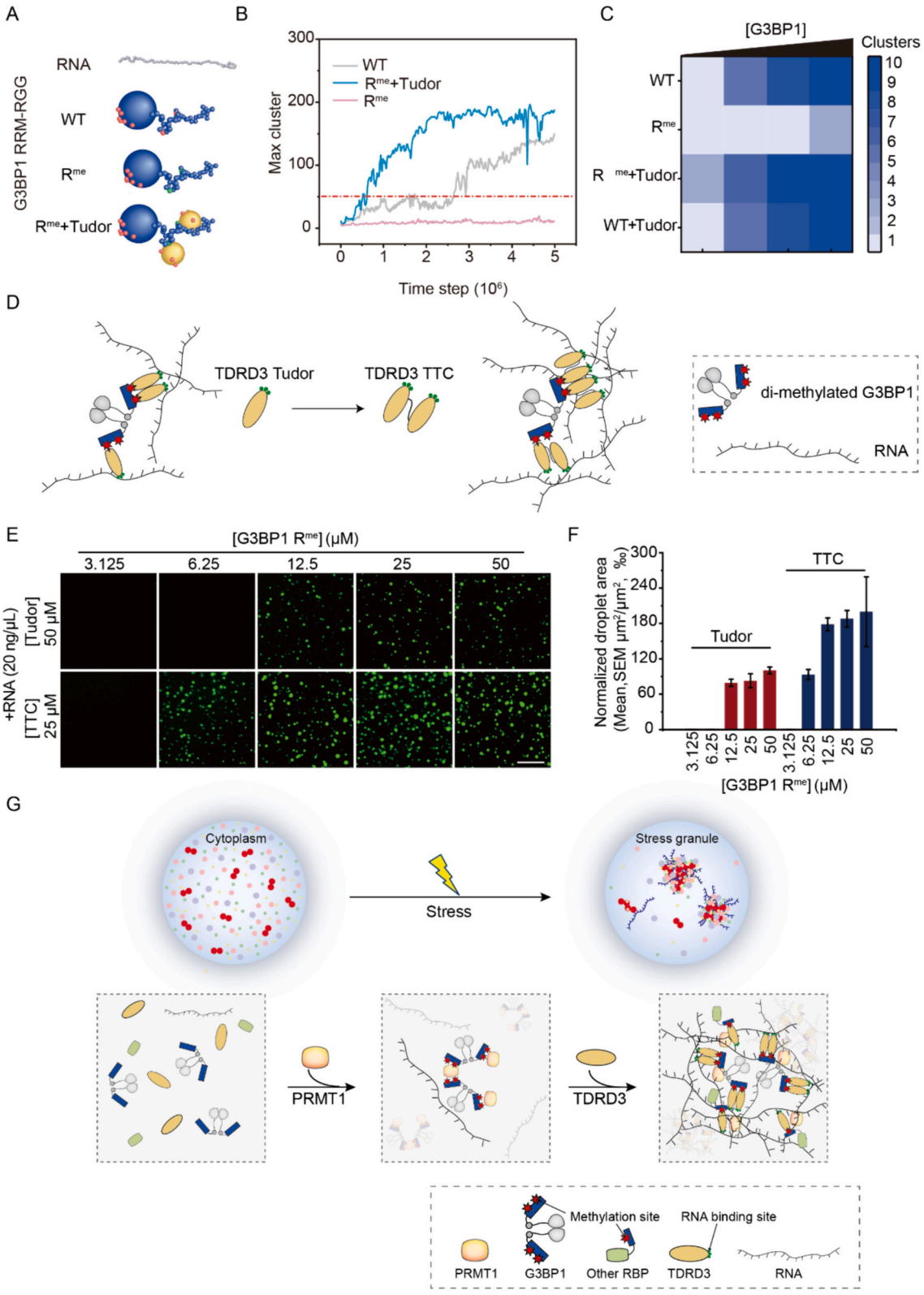

Fig. 4. TDRD3 enhances G3BP1-RNA interaction valence.
(A) Schematic of the G3BP1-TDRD3-RNA model, simulating G3BP1 RGG at a coarse-grained level, and representing G3BP1 RRM and TDRD3 Tudor domain as rigid bodies. (B) Variation in maximum cluster size within simulated systems. (C) Equilibrium molecular dynamics (MD) configurations of (un)methylated G3BP1-RNA with or without TDRD3 Tudor domain. (D) Schematic illustrating how tandem Tudor chimera (TTC) increases RNA-binding sites. (E, F) LLPS of G3BP1 R^{me} (50 μM) and RNAs (20 ng/μL) with a single TDRD3 Tudor domain (50 μM) or the TTC (25 μM). Scale bar, 20 μm. The droplet ratio is quantified in F, with n = 16. Error bars indicate SEM. (G) Model of PRMT1 and TDRD3 promote SG assembly by rebuilding the protein-RNA interaction network.

procedures 48 h after the initial siRNA transfection.

5.2. Arsenite addition and washout experiment, small-molecule treatment

For arsenite treatment, cells were stressed with 500 μM sodium arsenite in fresh medium at 37 °C for 60 min. As shown in Fig. S1B, cells were collected or observed at different time points. Each time point represents: 0 min, without treatment with sodium arsenite; 30 min, treatment with 500 μM sodium arsenite for 30 min; 60 min, treatment with 500 μM sodium arsenite for 60 min; 240 min, treatment with 500 μM sodium arsenite for 60 min and then released by washing out for 180 min in fresh medium.

For small-molecule treatment, MS023 (Med Chem Express, China, 1,831,110–54-3) was used to treat U2OS cells at 50 μM for 48 h.

5.3. Plasmids and antibodies

The genes encoding human TAF15, DDX3X, Caprin1, and UBAP2 were cloned into the pKH3 vector with an N-terminal HA tag. The genes encoding the human PRMT1 protein or the enzyme activity deficient mutant PRMT1 G80R were cloned into the p3xFLAG-Myc-CMV-24 vector with an N-terminal 3xFlag tag. The genes encoding the human TDRD3 wild-type or N596A mutant protein were cloned into the pcDNA3.1 vector with a C-terminal mCherry tag. The gene encoding human G3BP1 was cloned into the pKH3 vector with an N-terminal HA tag and the p3xFLAG-Myc-CMV-24 vector with an N-terminal 3xFlag tag. The gene encoding mutant G3BP1 (R435K/R447K) was cloned into the p3xFLAG-Myc-CMV-24 vector with an N-terminal 3xFlag tag.

Anti-PRMT1 (A33) antibody was purchased from Cell Signaling Technology (Shanghai, China, 2449S; 1:100 dilution for IF, 1:1000 dilution for WB). Anti-G3BP1 (*H*−10) antibody was purchased from Santa Cruz (Shanghai, China, sc-365,338; 1:100 dilution for IF). Anti-Flag antibodies were purchased from Proteintech (Wuhan, China, 20,543–1-AP; 1:1000 dilution for WB) and Sigma–Aldrichd (Shanghai, China, F1804; 1:100 dilution for IF, 2–4 μg for IP). Anti-HA antibodies were purchased from Proteintech (Wuhan, China, 66,006–2-Ig, 2–4 μg for IP; 51,064–2-AP, 1:1000 dilution for WB). Anti-ADMA antibody was purchased from ImmuneChem (Burnaby, British Columbia V5J3J1 Canada, ICP0810; 1:500 dilution for WB). Anti-TDRD3 antibody was purchased from Proteintech (Wuhan, China, 13,359–1-AP; 1:1000 dilution for WB). Anti-GAPDH antibody was purchased from Proteintech (Wuhan, China, 60,004–1-Ig; 1:10000 dilution for WB). Anti-Actin antibody was purchased from Proteintech (Wuhan, China, 81,115–1-RR; 1:10000 dilution for WB). Host-specific Alexa Fluor 488/594-conjugated secondary antibodies (Proteintech, Wuhan, China) were used for IF.

5.4. Co-immunoprecipitation

HEK293T or U2OS cells were transfected with the indicated plasmids, collected, and lysed in lysis buffer (Beyotime, Shanghai, China, P0013) containing 0.1 % Triton X-100 in the presence of a mammalian protease inhibitor cocktail (Sigma-Aldrich, Shanghai, China, P8340). After clarification by centrifugation, cell lysates were incubated with a corresponding antibody overnight at 4 °C with rotation and then incubated with protein A/G microbeads (Santa Cruz, Shanghai, China, sc-2003) for 3 h at 4 °C with rotation. After incubation, the beads were washed five times with lysis buffer containing 0.1 % Triton X-100 and then boiled in SDS-polyacrylamide gel electrophoresis (SDS–PAGE) sample buffer. The bound proteins were separated on an SDS–PAGE gel and transferred onto a nitrocellulose membrane for western blot analysis.

5.5. Imaging of SGs in cells

For the immunofluorescence study, U2OS cells were cultured on 20 mm × 20 mm glass coverslips coated with poly-D-lysine (Sigma–Aldrich, Shanghai, China, ST508) and placed in 35 mm dishes (Wuxi NEST Biotechnology Co., Ltd., Wuxi, China). Transfected cells were sequentially fixed with 4 % paraformaldehyde (Electron Microscopy Science, Beijing, China) in PBS for 10 min, permeabilized with 0.2 % Triton X-100 in PBS for 10 min, and blocked with 1 % BSA for 30 min, with all steps performed at room temperature. Samples were further incubated with primary antibodies in a blocking buffer overnight at 4 °C, washed three times with PBST (0.1 % Tween), and incubated with a secondary antibody for 1 h at room temperature. Then, 4,6-diamidino-2-phenylindole (DAPI) was used to visualize nuclei.

Images were acquired with a Nikon Ti confocal microscope with 445-nm, 488-nm, and 594-nm lasers. Additionally, Fig. 2A and E were acquired by LSM880 (Zeiss) with 405-nm, 488-nm, and 594-nm lasers. The same types of images were acquired with the same laser power and exposure time, shown under the same B&C ratio and enlarged to the same scale to make them comparable.

5.6. Cloning, protein expression, and purification

Purification of the proteins were similar with our previous work [55]. In short, G3BP1 RRM-RGG (327–466), TDRD3 Tudor (555–608) and their mutants were insert into the pET-28a vector with a 6 × His tag at N terminal. Proteins were overexpressed in *Escherichia coli* BL21 at 37 °C, inducing by 0.5 mM IPTG for 6 h. The buffer for purification was 2 M NaCl and 20 mM NaH_2PO_4, with pH 6.5. Nickel affinity columns (QIAGEN, Shanghai, China) and HiLoad 16/600 Superdex 75 column (GE Healthcare, Shanghai, China) were used to purify proteins. The methylated G3BP1 RRM-RGG (R^{me}).was acquired showed in our work [55].

5.7. His pull-down

His-G3BP1 RRM-RGG or that expressing with PRMT1 (10 μL, 0.1 mM) was mixed with label-free TDRD3 Tudor domain (10 μL, 0.1 mM) at 4 °C in Ni-PBS buffer (150 mM NaCl, 20 mM NaH_2PO_4, pH 6.5) for 1 h. The nickel affinity resin (10 μL, QIAGEN, Shanghai, China) was then added, washed with 20 μL Ni-PBS buffer with an additional 50 mM imidazole, and finally analyzed by SDS-PAGE.

5.8. Isothermal titration calorimetry (ITC) assay

The experiment was conducted using a MicroCal PEAQ-ITC instrument at a temperature of 25 °C. The buffer contained 150 mM NaCl and 20 mM Tris, with pH = 7.5. The peptides $R447^{me2a}$ (GPPR^{me2a}GGMVQK) and its unmethylated counterpart (GPPRGGMVQK) were synthesized by Tsingke Biotechnology Co., Ltd. (Nanjing, China). The concentration of the G3BP1 peptide was 3.8 mM, which was incrementally added to the TDRD3 Tudor domain at a concentration of 0.1 mM, with each addition consisting of 2 μL. The MicroCal PEAQ-ITC Analysis Software was employed to fit the binding affinity of the peptides to the TDRD3 Tudor domain using the one-site binding model.

5.9. NMR spectroscopy and titration

Nuclear magnetic resonance (NMR) spectroscopy is a useful technique for identifying interactions between molecules at an atomic level. In particular, the $^{1}H^{15}N$-HSQC spectrum generated by NMR can indicate the presence of amino acids, with each peak corresponding to a particular amino acid. During titration experiments, changes in the spectral peaks of amino acids can reveal residues involved in direct interactions. The chemical shift perturbations (CSPs) were calculated as:

$$\Delta = \sqrt{\frac{\Delta_H^2 + 0.04\Delta_N^2}{2}}$$

where Δ was the total CSPs and Δ_H and Δ_N were the CSPs of the ^{1}H and ^{15}N dimensions, respectively.

20 nt poly(A), poly(C), poly(U) and CAACUCU were synthesized by Accurate Biotechnology (Hunan) Co., Ltd., Hunan, China.

5.10. Liquid-liquid phase separation assay and its quantification

Similar with our previous work [55], all components were dissolved in the buffer with 150 mM NaCl, 20 mM NaH2PO4 and pH at 6.5. Alexa Fluor 488 NHS (Themo Fisher Shanghai, China, A10169) was used to label the N-termini of G3BP1 RRM-RGG. An LSM710 (Zeiss) microscope was used to acquire LLPS images.

The LLPS and SG area ratio were calculated as

$$\text{Ratio} = \frac{S_g}{S_t}$$

where S_g is the area of the droplets and S_t is the total area of the visual field [46–50].

5.11. Molecular dynamics simulation

In this study, we employed a multiscale coarse-grain method for the simulation of the RRM-RGG protein, wherein a residue-based resolution commonly applied for IDR was utilized for the disordered RGG region (residues 425–466), with each bead of $r_{res} = 0.19$ nm representing an amino acid [75,76]. The RRM domain (327–424) is modeled as a spherical rigid body of $r_{RRM} = 2.3$ nm with 6 interaction sites on the surface, the relative positions of which were mapped from the 3D structure of RRM and the sites were determined according to the NMR data for the interacting amino acids. Similarly, TDRD3 was treated as a spherical rigid body of $r_{TDRD} = 2.3$ nm with 3 interaction sites on the surface [77]. RNA chains were modeled at single-nucleotide resolution, with $r_{nt} = 0.35$ nm and 150 beads in each chain All simulations were performed in a cubic box of length $l_{box} = 100$ nm with periodic boundary conditions using reduced units of $k_BT = 1.0$. The simulations were performed for four different protein concentrations (100, 200, 300 and 400 chains), with a fixed RNA concentration of 40 chains.

The potential energy function contains exclusive volume, bonded, and electrostatic interaction terms. Exclusive volume effects among residue/nucleotide and domains are modeled using a spring potential $U_{ev} = k_{ev}(r-\sigma)^2, r < \sigma$, where $k_{ev} = 50.0$ and σ is the sum of a particular pair of particle radii. Bonded interactions are modeled by a harmonic potential $k_{\text{bond}}(r-r_0)^2$, with $k_{bond} = 100.0$ and an equilibrium bond length of $r_{0_{res}} = 0.38$ nm for proteins and $r_{0_{nt}} = 0.70$ nm for RNA. A harmonic angular term $k_{\text{angle}}(\theta-\theta_0)^2$ is added on RNA to reflect the stiffness of the RNA chains, where spring constant $k_{\text{angle}} = 2.0$ and equilibrium angle $\theta_0 = 180^\circ$ [78]. Electrostatic interactions among the interaction sites are modeled using a Coulombic term with Debye-Hückel electrostatic screening to account for the salt concentration, and the equation has the functional form

$$E = \frac{Cq_iq_j}{r} exp(-\kappa r), r < r_{cut}$$

where κ=0.1 is the inverse of the Debye screening length, $C = 5.0$ is a function of the dielectric constant of the solvent water, and r_{cut} is set as 3σ. Overdamped Langevin dynamics was applied for RNA and proteins:

$$\gamma \dot{r}_i = F_i(t) + \xi(t)$$

where $F_i(t)$ is the total potential energy of particle i mentioned above; $\dot{r}_i$ is the velocity of particle i; γ is the friction coefficient due to the solvent environment and was set as 0.5 and 0.25 for residue beads and rigid bodies, respectively; and ξ_i is the thermal noise with $< \xi_i(t)\xi_j(t') >= 2D1\delta_{ij}\delta_{tt'}$, where 1 is the unit tensor and $D = k_BT/\gamma$ is the diffusion constant. The simulation was performed with 1×10^5 equilibration steps followed by 5×10^7 running steps with an integration time step of 0.001 τ, where τ is the characteristic time scale for the coarse-grained system. All simulations were performed on RTX3080 graphics processing units (GPUs).

Clusters (droplets) were identified using the distance between domains, with a cutoff distance of 7.0 nm, *i.e.*, any two domain particles with a center-to-center distance of <7.0 nm were considered to be part of the same cluster. A cluster with a size >50 was regarded as a phase-separated droplet. A distance cutoff of 0.55 nm between RNA beads and protein interaction sites was used for valence calculations. All simulation snapshots were generated using OpenGL.

CRediT authorship contribution statement

Mengtong Qin: Writing – review & editing, Writing – original draft, Visualization, Validation, Methodology, Investigation, Formal analysis, Data curation. **Weiwei Fan:** Writing – review & editing, Writing – original draft, Visualization, Validation, Methodology, Investigation, Formal analysis. **Linge Li:** Software, Methodology. **Tian Xu:** Validation, Methodology. **Hanyu Zhang:** Validation. **Feng Chen:** Investigation. **Jingwen Man:** Methodology. **Arnaud John Kombe Kombe:** Writing – review & editing. **Jiahai Zhang:** Resources. **Yunyu Shi:** Supervision. **Xuebiao Yao:** Supervision. **Zhenye Yang:** Funding acquisition, Conceptualization. **Zhonghuai Hou:** Funding acquisition, Conceptualization. **Ke Ruan:** Project administration, Funding acquisition, Conceptualization. **Dan Liu:** Project administration, Funding acquisition, Conceptualization.

Declaration of competing interest

The authors declare that they have no known competing financial interests or personal relationships that could have appeared to influence the work reported in this paper.

Data availability

All data are available in the main text or the supplemental information.

Acknowledgments

This work was supported by the National Natural Science Foundation of China (32090041, 91749125, 21778050, 22377119, 32370776, 32090044), the National Key Research and Development Program of China (2016YFA0101200, 2019YFA0508400, 2022YFA1303100), the Collaborative Innovation Program of Hefei Science Center, CAS (2020HSC-CIP009), the Anhui Provincial Natural Science Foundation (2108085J12).

Appendix A. Supplementary data

Supplementary data to this article can be found online at https://doi.org/10.1016/j.ijbiomac.2024.134411.

References

[1] S.F. Banani, et al., Biomolecular condensates: organizers of cellular biochemistry, Nat. Rev. Mol. Cell Biol. 18 (5) (2017) 285–298.
[2] D.L. Spector, SnapShot: cellular bodies, Cell 127 (5) (2006) 1071.
[3] E. Dolgin, What lava lamps and vinaigrette can teach us about cell biology, Nature 555 (7696) (2018) 300–302.
[4] E. Dolgin, Cell biology's new phase like oil in water, the contents of cells can separate into droplets. Finding out why is one of biology's hottest questions, Nature 555 (7696) (2018) 300–302.
[5] C. Mathieu, R.V. Pappu, J.P. Taylor, Beyond aggregation: pathological phase transitions in neurodegenerative disease, Science 370 (6512) (2020) 56–60.
[6] S. Alberti, A.A. Hyman, Biomolecular condensates at the nexus of cellular stress, protein aggregation disease and ageing, Nat. Rev. Mol. Cell Biol. 22 (3) (2021) 196–213.

[7] A.S. Lyon, W.B. Peeples, M.K. Rosen, A framework for understanding the functions of biomolecular condensates across scales, Nat. Rev. Mol. Cell Biol. 22 (3) (2021) 215–235.
[8] P. Li, et al., Phase transitions in the assembly of multivalent signalling proteins, Nature 483 (7389) (2012) 336–340.
[9] S.F. Banani, et al., Compositional control of phase-separated cellular bodies, Cell 166 (3) (2016) 651–663.
[10] K.A. Burke, et al., Residue-by-residue view of in vitro FUS granules that bind the C-terminal domain of RNA polymerase II, Mol. Cell 60 (2) (2015) 231–241.
[11] S. Wegmann, et al., Tau protein liquid-liquid phase separation can initiate tau aggregation, EMBO J. 37 (7) (2018) e98049.
[12] C. Wang, et al., Stress induces dynamic, cytotoxicity-antagonizing TDP-43 nuclear bodies via paraspeckle LncRNA NEAT1-mediated liquid-liquid phase separation, Mol. Cell 79 (3) (2020) 443–458.e7.
[13] M. Ghosh, M. Singh, RGG-box in hnRNPA1 specifically recognizes the telomere G-quadruplex DNA and enhances the G-quadruplex unfolding ability of UP1 domain, Nucleic Acids Res. 46 (19) (2018) 10246–10261.
[14] C. Maris, C. Dominguez, F.H. Allain, The RNA recognition motif, a plastic RNA-binding platform to regulate post-transcriptional gene expression, FEBS J. 272 (9) (2005) 2118–2131.
[15] P.A. Chong, R.M. Vernon, J.D. Forman-Kay, RGG/RG motif regions in RNA binding and phase separation, J. Mol. Biol. 430 (23) (2018) 4650–4665.
[16] B. Van Treeck, R. Parker, Emerging roles for intermolecular RNA-RNA interactions in RNP assemblies, Cell 174 (4) (2018) 791–802.
[17] B. Van Treeck, et al., RNA self-assembly contributes to stress granule formation and defining the stress granule transcriptome, Proc. Natl. Acad. Sci. U. S. A. 115 (11) (2018) 2734–2739.
[18] P. Ivanov, N. Kedersha, P. Anderson, Stress Granules and Processing Bodies in Translational Control, Cold Spring Harb. Perspect. Biol. 11 (5) (2019).
[19] B.A. Maxwell, et al., Ubiquitination is essential for recovery of cellular activities after heat shock, Science 372 (6549) (2021) p. eabc3593.
[20] E.W. Wallace, et al., Reversible, specific, active aggregates of endogenous proteins assemble upon heat stress, Cell 162 (6) (2015) 1286–1298.
[21] K. Arimoto-Matsuzaki, H. Saito, M. Takekawa, TIA1 oxidation inhibits stress granule assembly and sensitizes cells to stress-induced apoptosis, Nat. Commun. 7 (2016) 10252.
[22] H. Mahboubi, U. Stochaj, Cytoplasmic stress granules: dynamic modulators of cell signaling and disease, BBA Molecular Basis of Disease 1863 (4) (2017) 884–895.
[23] L. Chen, B. Liu, Relationships between stress granules, oxidative stress, and neurodegenerative diseases, Oxid. Med. Cell. Longev. 2017 (2017) 1809592.
[24] S. Hofmann, et al., Molecular mechanisms of stress granule assembly and disassembly, Biochim. Biophys. Acta Mol. Cell Res. 1868 (1) (2021) 118876.
[25] N. Kedersha, P. Ivanov, P. Anderson, Stress granules and cell signaling: more than just a passing phase? Trends Biochem. Sci. 38 (10) (2013) 494–506.
[26] Y. Baradaran-Heravi, C. Van Broeckhoven, J. van der Zee, Stress granule mediated protein aggregation and underlying gene defects in the FTD-ALS spectrum, Neurobiol. Dis. 134 (2020) 104639.
[27] R. Gutierrez-Garcia, et al., G3BP1-dependent mechanism suppressing protein aggregation in Huntington's models and its demise upon stress granule assembly, Hum. Mol. Genet. 32 (10) (2023) 1607–1621.
[28] P. Adjibade, et al., Sorafenib, a multikinase inhibitor, induces formation of stress granules in hepatocarcinoma cells, Oncotarget 6 (41) (2015) 43927–43943.
[29] A. Vilas-Boas Fde, et al., Impairment of stress granule assembly via inhibition of the eIF2alpha phosphorylation sensitizes glioma cells to chemotherapeutic agents, J. Neurooncol 127 (2) (2016) 253–260.
[30] W. Szaflarski, et al., Vinca alkaloid drugs promote stress-induced translational repression and stress granule formation, Oncotarget 7 (21) (2016) 30307–30322.
[31] S.P. Somasekharan, et al., YB-1 regulates stress granule formation and tumor progression by translationally activating G3BP1, J. Cell Biol. 208 (7) (2015) 913–929.
[32] T. Hu, et al., Mechanism and effect of stress granule formation in cancer and its potential roles in breast cancer therapy, Genes Dis. 9 (3) (2022) 659–667.
[33] H. Liu, et al., SARS-CoV-2 N protein antagonizes stress granule assembly and IFN production by interacting with G3BPs to facilitate viral replication, J. Virol. 96 (12) (2022) e0041222.
[34] D.S.W. Protter, R. Parker, Principles and properties of stress granules, Trends Cell Biol. 26 (9) (2016) 668–679.
[35] M.D. Panas, P. Ivanov, P. Anderson, Mechanistic insights into mammalian stress granule dynamics, J. Cell Biol. 215 (3) (2016) 313–323.
[36] J. Guillen-Boixet, et al., RNA-induced conformational switching and clustering of G3BP drive stress granule assembly by condensation, Cell 181 (2) (2020) 346–361 e17.
[37] A. Khong, et al., The stress granule transcriptome reveals principles of mRNA accumulation in stress granules, Mol. Cell 68 (4) (2017) 808–820 e5.
[38] P. Yang, et al., G3BP1 is a tunable switch that triggers phase separation to assemble stress granules, Cell 181 (2) (2020) 325–345 e28.
[39] Y. Gwon, et al., Ubiquitination of G3BP1 mediates stress granule disassembly in a context-specific manner, Science 372 (6549) (2021) p. eabf6548.
[40] W.C. Tsai, et al., Arginine demethylation of G3BP1 promotes stress granule assembly, J. Biol. Chem. 291 (43) (2016) 22671–22685.
[41] L. Huang, et al., Arginine methylation of the C-terminus RGG motif promotes TOP3B topoisomerase activity and stress granule localization, Nucleic Acids Res. 46 (6) (2018) 3061–3074.
[42] C. Chen, et al., Deciphering arginine methylation: Tudor tells the tale, Nat. Rev. Mol. Cell Biol. 12 (10) (2011) 629–642.
[43] Y. Yang, et al., TDRD3 is an effector molecule for arginine-methylated histone marks, Mol. Cell 40 (6) (2010) 1016–1023.
[44] M. Ahmad, D. Xu, W. Wang, Type IA topoisomerases can be "magicians" for both DNA and RNA in all domains of life, RNA Biol. 14 (7) (2017) 854–864.
[45] I. Goulet, et al., TDRD3, a novel Tudor domain-containing protein, localizes to cytoplasmic stress granules, Hum. Mol. Genet. 17 (19) (2008) 3055–3074.
[46] P. Choudhury, L.D. Bussiere, C.L. Miller, Mammalian orthoreovirus factories modulate stress granule protein localization by interaction with G3BP1, J. Virol. 91 (21) (2017) p. e01298–17.
[47] S. Markmiller, et al., Active protein neddylation or ubiquitylation is dispensable for stress granule dynamics, Cell Rep. 27 (5) (2019) 1356–1363 e3.
[48] P. Lv, et al., O-GlcNAcylation modulates liquid-liquid phase separation of SynGAP/PSD-95, Nat. Chem. (2022) 831–840.
[49] B. Shi, et al., Phase separation of Ddx3xb helicase regulates maternal-to-zygotic transition in zebrafish, Cell Res. (2022) 715–728.
[50] M.Y. Fang, et al., Small-molecule modulation of TDP-43 recruitment to stress granules prevents persistent TDP-43 accumulation in ALS/FTD, Neuron 103 (5) (2019) 802–819.e11.
[51] N. Cheung, et al., Protein arginine-methyltransferase-dependent oncogenesis, Nat. Cell Biol. 9 (10) (2007) 1208–1215.
[52] H. Wang, et al., Methylation of histone H4 at arginine 3 facilitating transcriptional activation by nuclear hormone receptor, Science 293 (5531) (2001) 853–857.
[53] T. Sikorsky, et al., Recognition of asymmetrically dimethylated arginine by TDRD3, Nucleic Acids Res. 40 (22) (2012) 11748–11755.
[54] M. Deater, M. Tamhankar, R.E. Lloyd, TDRD3 is an antiviral restriction factor that promotes IFN signaling with G3BP1, PLoS Pathog. 18 (1) (2022) e1010249.
[55] W.W. Fan, et al., A bivalent inhibitor against TDRD3 to suppress phase separation of methylated G3BP1, Chem. Commun. (Camb.) 60 (6) (2024) 762–765.
[56] T. Sikorsky, et al., Recognition of asymmetrically dimethylated arginine by TDRD3, Nucleic Acids Res. 40 (22) (2012) 11748–11755.
[57] D.W. Sanders, et al., Competing protein-RNA interaction networks control multiphase intracellular organization, Cell 181 (2) (2020) 306–324 e28.
[58] G. Grimmett, Percolation, 2 ed., Springer Berlin, Berlin, 1999.
[59] T. Mittag, R.V. Pappu, A conceptual framework for understanding phase separation and addressing open questions and challenges, Mol. Cell 82 (12) (2022) 2201–2214.
[60] A.A. Deniz, Percolation physics and density transition frameworks converge in biomolecular condensation, Proc. Natl. Acad. Sci. U. S. A. 119 (32) (2022) p. e2210177119.
[61] H. Zhang, X. Tu, J. Zhang, (1)H, (13)C and (15)N resonance assignments of stress granule key component G3BP1 RRM domain, Biomol. NMR Assign. 16 (1) (2022) 109–111.
[62] A. Molliex, et al., Phase separation by low complexity domains promotes stress granule assembly and drives pathological fibrillization, Cell 163 (1) (2015) 123–133.
[63] J.R. Wheeler, et al., Distinct stages in stress granule assembly and disassembly, Elife (2016) 5.
[64] N. Kedersha, et al., G3BP-Caprin1-USP10 complexes mediate stress granule condensation and associate with 40S subunits, J. Cell Biol. 212 (7) (2016) 845–860.
[65] M. Deater, M. Tamhankar, R.E. Lloyd, TDRD3 is an antiviral restriction factor that promotes IFN signaling with G3BP1, PLoS Pathog. 18 (1) (2022) e1010249.
[66] S.M. Hou, et al., Zika virus hijacks stress granule proteins and modulates the host stress response, J. Virol. 91 (16) (2017) p. e00474–17.
[67] Q. Cui, et al., Diverse CMT2 neuropathies are linked to aberrant G3BP interactions in stress granules, Cell 186 (4) (2023) 803–820 e25.
[68] H. Sidibe, A. Dubinski, C. Vande Velde, The multi-functional RNA-binding protein G3BP1 and its potential implication in neurodegenerative disease, J. Neurochem. 157 (4) (2021) 944–962.
[69] B. Wolozin, P. Ivanov, Stress granules and neurodegeneration, Nat. Rev. Neurosci. 20 (11) (2019) 649–666.
[70] T. Vanderweyde, et al., Role of stress granules and RNA-binding proteins in neurodegeneration: a mini-review, Gerontology 59 (6) (2013) 524–533.
[71] H.J. Kim, J.P. Taylor, Lost in transportation: nucleocytoplasmic transport defects in ALS and other neurodegenerative diseases, Neuron 96 (2) (2017) 285–297.
[72] G. Halliday, et al., RNA-binding protein dysfunction in neurodegeneration, Essays Biochem. 65 (7) (2021) 975–986.
[73] L. Hagen, et al., Off-target responses in the HeLa proteome subsequent to transient plasmid-mediated transfection, Biochim. Biophys. Acta 1854 (1) (2015) 84–90.
[74] X. Guo, et al., Transfection reagent Lipofectamine triggers type I interferon signaling activation in macrophages, Immunol. Cell Biol. 98 (1) (2020) 88.
[75] G.L. Dignon, et al., Sequence determinants of protein phase behavior from a coarse-grained model, PLoS Comput. Biol. 14 (1) (2018).
[76] G.L. Dignon, et al., Relation between single-molecule properties and phase behavior of intrinsically disordered proteins, Proc. Natl. Acad. Sci. U. S. A. 115 (40) (2018) 9929–9934.
[77] J.R. Espinosa, et al., Liquid network connectivity regulates the stability and composition of biomolecular condensates with many components, Proc. Natl. Acad. Sci. U. S. A. 117 (24) (2020) 13238–13247.
[78] I. Alshareedah, et al., Phase transition of RNA-protein complexes into ordered hollow condensates, Proc. Natl. Acad. Sci. U. S. A. 117 (27) (2020) 15650–15658.